Biomedical Materials

ACCEPTED MANUSCRIPT • OPEN ACCESS

Application of high resolution DLP stereolithography for fabrication of tricalcium phosphate scaffolds for bone regeneration

Application of High Resolution DLP Stereolithography for Fabrication of Tricalcium Phosphate Scaffolds for Bone regeneration

Christina Schmidleithner[1], Sara Malferarri[1], Robert Palgrave[2], Daniel Bomze[3], Martin Schwentenwein[3], Deepak M. Kalaskar[1]

[1] Institute of Musculoskeletal sciences (IOMS), UCL Division of Surgery and Interventional Science, Royal National Orthopaedic Hospital-NHS Trust. Stanmore, Middlesex, HA7 4LP, United Kingdom
[2] Department of Chemistry, University College London, London, UK
[3] Lithoz GmbH, Mollardgasse 85a/2/64-69, 1060 Vienna, Austria

E-mail: xxx@xxx.xx

Abstract

Bone regeneration requires porous and mechanically stable scaffolds to support tissue integration and angiogenesis, which is essential for bone tissue regeneration. With the advent of additive manufacturing process, production of complex porous architecture has become feasible. However, a balance has to be sorted between porous architecture and mechanical stability which facilitates bone regeneration for load bearing applications.

Current study evaluates used of high resolution digital light processing (DLP) -based additive manufacturing to produce complex but mechanical stable scaffolds based on β-tricalcium phosphate (β-TCP) for bone regeneration.

Four different geometries, a rectilinear Grid, hexagonal Kagome, schwart primitive and hollow Schwarz are designed with 400 µm pores and 75 or 50 vol.% porosity. However after initial screening for design stability and mechanical properties, only a rectilinear Grid structure, a hexagonal Kagome structure are found to be reproducible and showed higher mechanical properties.

Micro computed tomography (µ-CT) analysis shows < 2 vol. % error in porosity and < 6 % relative deviation of average pore sizes for the Grid structures. At 50 vol. % porosity, this architecture also has the highest compressive strength of 44.7 MPa (Weibull modulus is 5.28), while bulk specimens reach 235 ± 37 MPa.

To evaluate suitability of 3D scaffolds produce by DLP methods for bone regeneration, scaffolds were cultured with murine preosteoblastic MC3T3-E1 cells. Short term study showed cells growth over 14 days, with more than two-fold increase of alkaline phosphatase (ALP) activity compared to cells on 2D tissue culture plastic. Collagen deposition was increased by a factor of $1.5 - 2$ when compared to the 2D controls. This confirm retention of biocompatible and osteo-inductive properties of β-TCP following DLP process.

This study has implications for designing of the high resolution porous scaffolds for bone regenerative applications and contributes to understanding of DLP based additive manufacturing process for medical applications.

1. Introduction

For large bone defects where native bone repair is insufficient and surgical intervention is required, bone tissue engineering (TE) has emerged as a promising alternative to conventionally used tissue grafts [1–3]. In TE, cells are combined with growth factors and scaffolds to generate new tissue. As one of the key components, the 3D support structures for this newly formed tissue need to fulfil certain requirements.

The scaffold material should not be toxic, elicit an immune response, or contain leachable toxins or degradation products, which might have negative long-term effects [4,5]. Biodegradability of the scaffold is advantageous if, once implanted, it degrades at a controlled rate corresponding to growth of newly formed bone. Scaffold properties such as mechanical strength should thereby be continually replaced as it is resorbed, ideally leading to full regeneration of function without foreign body reactions [5–7].

Biomechanical properties should, furthermore, be compatible with native tissue, exhibiting high enough compressive strength to replace the load bearing function while avoiding issues coinciding with exceedingly high stiffness such as stress concentration at interfaces or bone loss due to stress shielding [5,8]. Typical values of compact bone, which are highly dependent on porosity and density, are 100 - 180 MPa for compressive strength and 12 - 25 GPa for apparent E-modulus [9–11].

Scaffold permeability is just as vital to *in vivo* success. Cell migration and nutrient transportation require pores of $\geq 100\,\mu m$ [12] and when neovascularization is desired, a benchmark of 300 - 500 μm has been suggested [12–15]. When regarding β-TCP scaffolds, Feng *et al.* [16] have for instance shown that growth of blood vessels is limited when pore sizes of fall below 400 μm while Ghayor & Weber [17] found that pores larger than 1200 μm are detrimental for osteoconduction. However, porous architecture has an impact on the mechanical strength of the scaffold. Consequently, an optimum balance between porosity and mechanical strength needs to be achieved for bone tissue regeneration.

1.1 Calcium Phosphate Scaffolds

Synthetic or natural polymers have been widely employed as bone TE scaffolds. However, due to their low compressive strength and stiffness, they cannot replace the load bearing function of bone [18–20]. Bioactive glasses, although stronger than most polymeric biomaterials, can be associated with poor sinterability [21] and low fracture toughness [22].

Thus, ceramic scaffolds based on calcium phosphates such as hydroxyapatite (HA) or β-tricalicum phosphate (β-TCP) are considered. They are chemically similar to the inorganic component of bone, and are known to promote osteoblast adhesion, proliferation, and formation of extracellular matrix (ECM), *i.e* they are osteoconductive [23]. Bulk compressive strengths of these calcium phosphates have been reported in a wide range of 5 - 500 MPa [9], which hinders comparison of HA and β-TCP.

In its stoichiometric and crystalline form, HA only shows limited biodegradability, whereas β-TCP has faster dissolution kinetics [24,25]. This rationale substantiates the use of β-TCP when manufacturing biodegradable bone TE scaffolds.

1.2 Additive Manufacturing Processes

Scaffold topology can be precisely modified by employing additive manufacturing approaches in order to combine the prerequisite of permeability with desired high compressive strengths.

Commonly used methods for TCP scaffolds include extrusion based systems [26–29], where a ceramic paste is deposited through a nozzle in a predefined pattern. Solidification is followed by application of a next layer, incrementally building up the part. Besides the relatively low resolution of approximately 100-200 μm [30], certain design limitations exist due to the dimensions of the cylindrical material threads, which construct every xy-plane.

Selective laser sintering (SLS) has also been employed to fabricate TCP or biphasic calcium phosphate scaffolds [31,32]. In this process, a powder bed is exposed to a laser beam, which locally fuses a layer of the material. Although there are less design constraints than in extrusion based techniques and superior resolutions can be attained, disadvantages such as poor surface qualities or insufficient sintering densities remain [33,34].

TCP structures for TE have also been attained by binder jetting [35,36]. Here, the material in the powder bed is coalesced in a layer-by-layer fashion by a liquid binder solution. Similarly to SLS, poor mechanical properties due to remaining high porosities are, however, problematic [37].

Stereolithography (SLA) can also be employed to create calcium phosphate scaffolds [38,39]. These systems utilize a photocurable ceramic slurry, where each layer is cured by exposure to light. Subsequent thermal processing removes the organic binder phase and yields a dense specimen. The digital light processing (DLP) based exposure mechanism of the presently used system ensures simultaneous irradiation of the entire desired cross section, leading to shorter processing times when compared to laser illuminated SLA. Its main

advantage over other additive manufacturing systems is higher resolution [40,41]. DLP is being investigated extensively for manufacturing of calcium phosphate structures in bone tissue engineering [17,39,42] and this study provides first examples of the technology for fabrication of complex high resolution porous architectures and high strength scaffolds.

The current work focuses on the use of DLP SLA to fabricate 3D scaffolds of various porosities and geometries using β-TCP for applications in bone tissue regeneration. Four different geometries, a rectilinear Grid, hexagonal Kagome, schwart primitive and hollow Schwarz are designed with 400 µm pores and 75 or 50% porosity. However after initial screening for design stability and mechanical properties, only a rectilinear Grid structure, a hexagonal Kagome structure are found to be reproducible and showed higher mechanical properties and thus studied in detailed (please supplementary data for more details).

The rectilinear grid structure and hexagonal geometries of 50 and 75 % porosities were evaluated using compressive testing and micro CT to ascertain mechanical and structural properties respectively. Complete chemical analysis pre and post fabrication was carried out using XPS and XRD. Pre-osteoblast MC3T3 cells were used to evaluate biocompatibility of 3D printed scaffolds by DLP process and their ability to form bone in short term culture.

2. Materials and Methods

2.1 Scaffold Design

Out of four different scaffold designs were employed; schwart primitive and hollow Schwarz were not continued due to their low mechanical reproducibility and the fractures found in the Hollow Schwarz architectures after sintering (see supplementary data for more details). The rectilinear grid structure (G) and a hexagonal Kagome structure (K) were created with two different porosities; 50 vol.% (G50 and K50) and 75 vol.% (G75 and K75). Additionally, one non-porous bulk specimen (F0) was manufactured. Pore sizes were set to 400 µm and cubes of 6 mm edge length were built for general analysis, 5 mm cubes were used for cell culture experiments and 6x6x12 mm specimens were employed in compressive testing unless stated otherwise. The Computer Aided Design (CAD) of the G50 and G75 structures were created in the Simpleware CAD module (Synopsis®, Inc.) using the internal structure wizard. K50 and K75 unit cells were designed in SOLIDWORKS 2017 SP03 according to Zok *et al*. [43] and then propagated with the linear pattern function.

2.2 Sample Manufacturing

A ceramic additive manufacturing system CeraFab 7500 (Lithoz GmbH, Austria), as previously described in literature [40,41], was employed with a commercial LithaBone TCP 380D slurry. The β-TCP powder was suspended in an organic matrix consisting of acrylates and methacrylates with a radical photoinitiator absorbing in the blue visible region [44]. Thus, after selective exposure to visible light, the slurry is cured. In this DLP stereolithography approach, as shown in Figure 1 (a) – (e), a digital micromirror device acts as a dynamic mask by selectively enabling or disabling single mirrors of a large mirror array. While the pixel size is fixed to 40 µm in the lateral xy-plane by the dedicated optical system, the layer height in z-direction can be adjusted from 10 to 100 µm. For this study a layer height of 25 µm was selected due to considerations of build speed and part resolution.
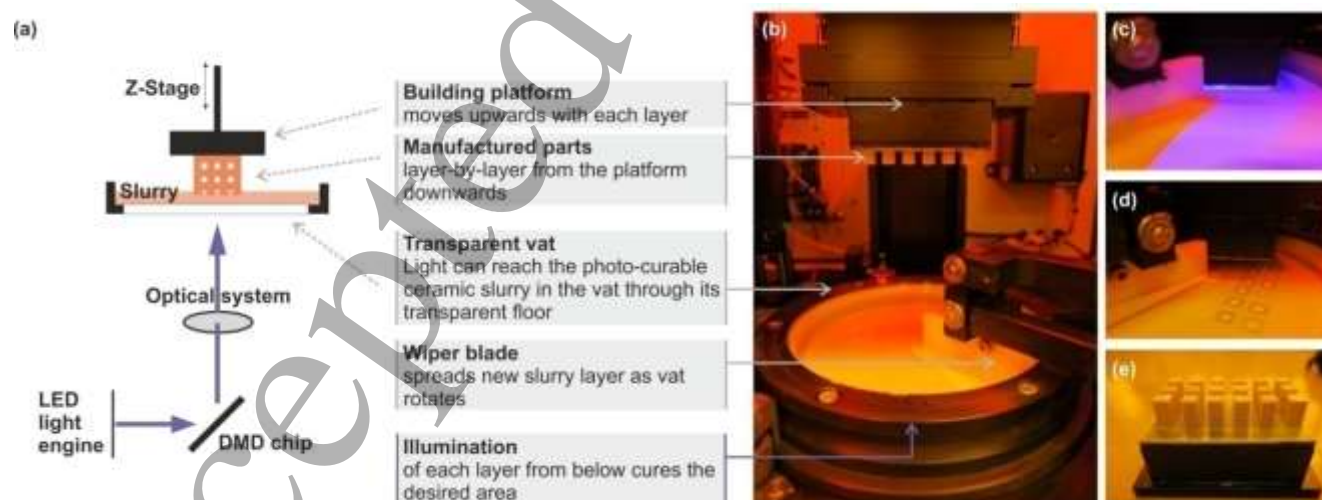

Figure 1: (a): Schematic of a DLP process redrawn from [45]. (b): photographs of the Lithoz CeraFab ceramic additive manufacturing system (LCM); (c): Illumination by DMD from below; (d): lifting-up of the building platform and recoating of the slurry layer; (e): completed green parts still on building platform.

The manufactured green parts were cleaned from excess uncured slurry by application of pressurized air, post cured in a UV chamber for 2 min and then thermally processed in a Nabertherm P330 furnace. Degradation of the organic matrix and its volatilization as well as sintering was conducted in a 96 h process at temperature rates which were varied between 0.17 and 0.52 °C min^{-1}. The maximum sintering temperature of 1200 °C was held for 2 h. All scaffold designs were treated with experimentally determined scaling factors prior to manufacturing to account for shrinkage during thermal treatment of 1.267 in x, y directions and of 1.281 in z direction. Over-polymerization during curing was also taken into account by scaling factors determined for each scaffold individually, as depicted in Table 1.

Table 1: Scaling factors for CAD of the scaffolds to account for reduced porosity and pore size.

Scaffold	Porosity	Pore Size
G75	1.107	1.188
G50	1.180	1.188
K75	1.060	1.150
K50	1.070	1.150

2.3 Micro Computed Tomography

A Bruker Skyscan 1172 micro-CT apparatus (Department of Cell and Developmental Biology, UCL) with a 0.5 mm aluminium filter was employed. Voltage was set to 50 kV and 200 µA current was used to measure and average 4 frames with 0.5° rotation steps and voxel sizes of 9 µm. Data was reconstructed in the NRecon (Bruker microCT) and internal dimensions were measured from these raw images. Four different locations within the scaffolds (at the centre and on the surface, in xy planes and in planes parallel to the z axis) were measured in quadruplicates. After processing in CT-Analyser 1.13 (Bruker-microCT), porosities were determined by considering volume of interests consisting only of complete unit cells.

2.4 Scanning Electron Microscopy (SEM)

SEM images were produced on a JEOL JSM-6301F system (Department of Chemistry, UCL) at a working distance of 7.5 – 8.0 mm and with applied voltage of 5.0 kV. To assure conductivity, samples were gold plasma coated for 1.5 min at 20 mA and connected to the carrier plate with a copper wire. Measurements of the images were taken in the ImageJ software and grain sizes were determined using the lineal intercept method according to Wurst & Nelson [46].

2.5 Density Measurements

Bulk density measurements were carried out on the non-porous F0 structures with the Archimedean method. A Sartorius density determination kit YDK 01 was used according to the manufacturer's specifications. Briefly, 5 replicate specimens were weighed 5 times in air and subsequently 5 times when immersed in water. The density of the sintered part could then be calculated from its mass and its buoyancy according to DIN EN 1389:2004-03 [47].

2.6 X-Ray Photoelectron Spectroscopy (XPS)

XPS measurements were carried out on powdered and homogenized samples with Al Kα radiation using a ThetaProbe MKII spectrometer (Thermo Scientific, Department of Chemistry, UCL) with an electron/ion flood gun. Spectra were acquired after 2 min of argon-ion etching to remove adventitious carbon. High resolution scans were taken at pass energies of 50 eV with steps of 0.100 eV. Calibration according to C 1s at 284.8 implemented in the CasaXPS software.

2.7 Powder X-Ray Diffraction (XRD)

Samples were crushed by pistil and mortar and the fine, homogeneous powder was packed into a 0.3 mm capillary. Powder XRD spectra were then acquired on a Stoe STADI-P system (Department of Chemistry, UCL) in transmission mode with Cu Kα$_1$ irradiation. The 2 θ range was 2.000 - 69.815° with 0.495° steps and scan rate was set to 10.0 s step^{-1}. Data analysis in the FullProf [48] software was carried out with starting parameters for β-TCP from [49] and for HA from [50].

2.8 Compression Testing

An in-house ZwickRoell Z005 compression machine was used for compressive testing according to ASTM standard D695-15 [51]. Crosshead speed was 1.3 mm min^{-1} in order to be within a representative region in alignment with speeds of 0.33 – 8 mm min^{-1} used in literature [27,37]. A pre-load of 10 N was applied prior to compression and samples were rectangular prisms with dimensions of 6x6x12 mm unless stated otherwise. At least 18 replicates were measured as fired, maximum stress at fracture was taken, and Weibull analysis was carried out according to Quinn & Quinn [52].

2.9 Culture of MC3T3-E1 Cells

Murine pre-osteoblastic MC3T3-E1 cells (Subclone 4, CRL-2593; ATCC, UK) were cultured in Minimum Essential Medium without ascorbic acid (α-MEM; A10490-01; Thermo Fisher Scientific Inc., UK). 10 % FCS as well as 1000 U mL^{-1} penicillin and streptomycin supplements were added and incubation was implemented at 37 °C in 5 % CO$_2$ atmosphere. Culture medium was renewed every 2 - 3 days and at 70 % confluency cells were passaged in a ratio of 1:6 by detaching with a 0.05 % trypsin/EDTA solution in PBS.

2.10 Cell Seeding

$2.25*10^5$ passage 3 cells were seeded per scaffold, which had been sterilized in 70 % ethanol. 30 µL of a $7.6*10^6$ cells mL^{-1} suspension were administered onto the scaffolds or to the 2D control wells. After resting at 25 °C for 15 min, 400 µL of α-MEM was added and the cells were incubated for 1 h. An additional 500 µL of medium was then included and a 12 h incubation period followed. Scaffolds were then transferred to clean wells in order to exclude any cells seeded on the well floors and the medium was replaced with osteogenic medium. α-MEM was additionally supplemented with 100 nM dexamethasone, 50 µg mL^{-1} ascorbic acid, and 10 mM β-glycerophosphate to yield the differentiation medium. Only one of the 2D conditions remained in the basal α-MEM. Subsequently, medium was changed every 2 - 3 days.

2.11 DNA Quantification

A Quanti-iT PicoGreen assay (P7589; Thermo Fisher Scientific Inc., UK) was utilized for DNA quantification according to the specifications. Cells were lyzed with 1 % Triton X-100 (Sigma Aldrich, USA) and after addition of the reagent, diluted 1:200 in the provided puffer solution. Fluorescence was recorded with excitation at 480 nm and emission at 520 nm. For quantification, a standard curve was prepared with MC3T3-E1 cells at passage 4. Measurements were taken at time points of day 1, 7, and 14.

2.12 Cell Staining

F-actin filaments were stained by Alexa Fluor 594 phalloidin (A12381; Thermo Fisher Scientific Inc., UK) and counterstaining of DNA was carried out by 4', 6-diamidino-2-phenylindole dihydrochloride (DAPI; D1306; Thermo Fisher Scientific Inc., UK) according to the manufacturers' specifications. An in-house ApoTome.2 fluorescence microscope (Carl Zeiss Microscopy GmbH) was utilized for imaging. Images were taken after 1, 7, and 14 days of cell culturing.

2.13 Alkaline Phosphatase Activity (ALP)

The Alkaline Phosphatase assay (ab83369; Abcam, UK) was used according to the manufacturer's specifications at 1, 7, and 14 days of cell culture. Briefly, Para-nitrophenylphosphate (pNPP) was employed as a substrate to asses ALP activity and optical density (OD) was recorded at 405 nm.

2.14 Collagen Deposition

A Sircol Soluble Collagen assay (S1000; Biocolor, UK) was employed for quantification of total collagen deposition at days 7 and 14. The assay was not feasible as suggested from the manufacturer, as TCP dissolved in the isolation reagents and subsequently interfered with the measurements. An alternative protocol was used [53] where the specimens were fixed in methanol at -20 °C over night and then directly exposed to 1 mL Sircol dye for 4 h at 25 °C. After washing in PBS and in 0.1 % acetic acid, images were taken with a reflective light microscope (Zeiss Stemi 508). For quantification, the dye was dissolved in 250 µL of the alkali reagent and 100 µL of the solution was placed in 96 well plates to measure absorbance at 555 nm.

2.15 Statistical analysis

All cell culture experiments were analyzed after subtraction of negative controls. Data were taken from 3 sample replicates, measured in duplicates, and given as mean ± standard deviation (SD). Statistical significance was evaluated by analysis of variance (ANOVA) or the Student's t-test in SigmaPlot 12.0. At $P < 0.005$, statistical significance was acknowledged and at $P < 0.001$, data were declared as highly significant.

3. Results and Discussions

3.1 Analysis of Manufactured Geometries

Rectilinear Grid structures and hexagonal Kagome structures were fabricated in 50 and 75 vol.% porosities according to the CADs displayed in Figure 2 (a) and (b). While unit cell size as well as strut thickness varied across the different designs, smallest pore diameter was chosen as a fixed parameter at 400 µm. This value was selected as it is at the lower limit of pore sizes necessary to enable neovascularization [12,13,16]. µ-CT data, compare Figure 2 (c), shows all scaffolds exhibiting complete interconnected porosity and homogeneous pore architecture. Pore dimensions deviated from the desired 400 µm by less than 6 % (Figure 2 (d)) and the unit cell dimensions (Figure 2 (e)) of all architectures correspond to the CAD with a relative error of less than 2 %. This high accuracy was achieved due to the employment of experimentally determined scaling factors and the reproducible nature of the LCM manufacturing process. When regarding the porosity of the scaffolds in Figure 2 (f), it is noticeable that the Grid architectures correlate better to the desired values with maximum relative deviations 3 % than the Kagome scaffolds. The latter showed deviations from specifications of up to 16 %. The source of this reduced porosity could be over-curing of the organic matrix caused by scattered light during the manufacturing process. When the energy threshold needed for polymerization is exceeded, curing can occur even outside of the designated area [54]. In the more intricate Kagome architecture, this phenomenon does not scale linearly with porosity as it does for the Grid structure, necessitating a more complex approximation.

SEM images in Figure 2 (g) and (h), show nonhomogeneous surface with the 20 ± 2 µm ridges stemming from the layer-by-layer technique of the additive

manufacturing process and grain sizes of $3.83 \pm 0.48 \, \mu m$ are identified (Figure 2 (i)). Furthermore, the visually compact microstructure, as inferable from the absence of intergranular pores, is confirmed by density values of $3.050 \pm 0.006 \, g \, cm^{-3}$ (99.5 % of crystallographic density [55]) obtained from Archimedean measurements of bulk specimens. This high

strut density is vital for the scaffolds' mechanical integrity. Especially for ceramics, high density can be correlated to a low amount of flaws in the microstructure, which leads to high strength materials [56,57].
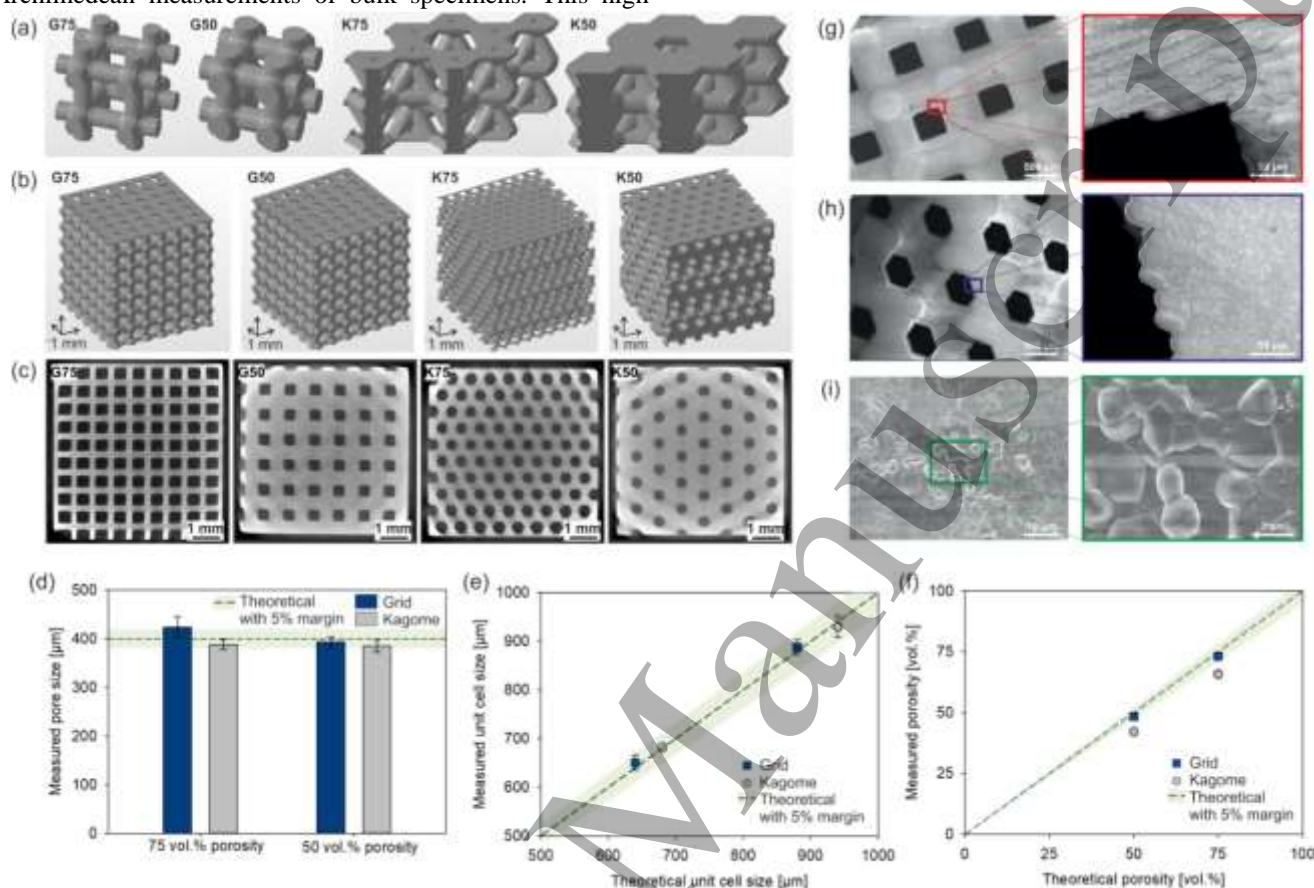

Figure 2: (a): CAD of an assembly of 8 unit cells for the Grid structures and 1 unit cell for the Kagome structures; not to scale. (b): CAD of 6 mm cubes of the four scaffold types. (c): μ-CT slices in the x, y-plane of the scaffolds after filtering. (d): Measured pore sizes from μ-CT images plotted against theoretical dimensions according to CAD (n = 16, ± SD). (e): Measured unit cell sizes according to μ-CT images (n = 16, ± SD). (f): Measured porosities of the scaffolds form thresholded μ-CT data plotted against theoretical porosity according to CAD. (g): SEM images of G50 structures. (h): SEM images of K50 structures. (i): Higher magnification SEM images of the F0 structure.

3.2 Validation of β-TCP Purity

XPS spectra in Figure 3 (a) show high purity of the TCP material before and after the 3D printing process. All organic components introduced as the binder phase during manufacturing are removed in the thermal processing step, as indicated by disappearance of the C 1s peak. This is beneficial

as it eliminates potential cytotoxicity issues often associated with (meth-)acrylate chemistry [58,59].

The calcium (Ca) to phosphorous (P) ratio of stoichiometric TCP is 1.50. The present material, however, exhibits a slight calcium deficiency, compare Table 2. Calcium vacancies [60] or traces of magnesium substitutions [61] are common explanations of this phenomenon.
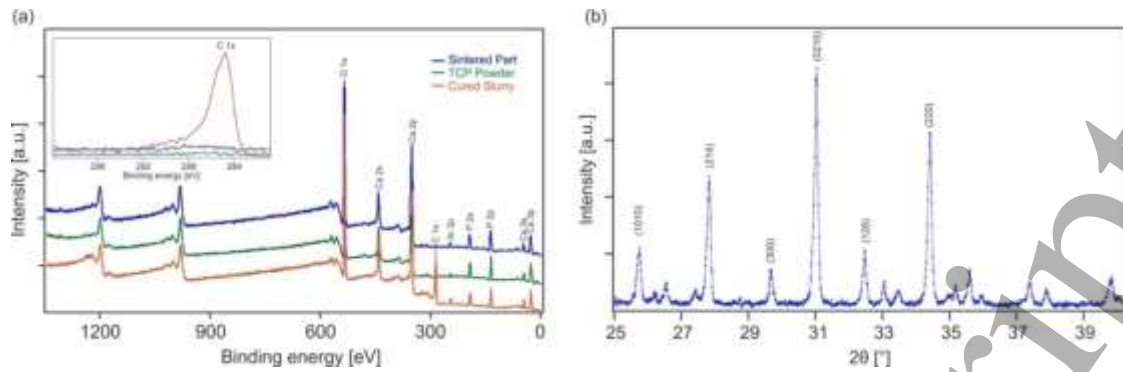
Figure 3: (a): XPS measurements of a manufactured part after binder removal and sintering, of the β-TCP powder prior to manufacturing, and of cured slurry. Measurements were taken after 2 min of argon-ion beam etching. (b): Section of XRD spectra of manufactured part after binder removal and sintering

Table 2: Peak positions and atomic ratios of elements in XPS spectra of cured slurry, of β-TCP powder prior to processing, and of sintered part. The C 1s peak is only listed for the cured slurry as no carbon is present in the purely ceramic specimens.

Sample	C 1s		P 2p		Ca 2p		O 1s		Ca/P ratio
	[eV]	[%at]	[eV]	[%at]	[eV]	[%at]	[eV]	[%at]	
Cured slurry	284.8	35.06	133.0	11.03	346.6	18.44	530.7	35.48	1.67
TCP powder	-	-	133.1	19.01	346.8	27.06	530.7	53.92	1.42
Sintered part	-	-	132.9	18.60	346.8	27.03	530.5	54.37	1.45

The XRD spectrum of the sintered specimens in Figure 3 (b) confirms high purity and crystallinity of β-TCP without traces of HA or any other phases. Benefits of the demonstrated high purity and absence of amorphous phases are not limited to considerations of cytotoxicity and mechanical integrity but are also a prerequisite for reproducible degradation rates, which are greatly dependent on stoichiometry and crystallinity [62].
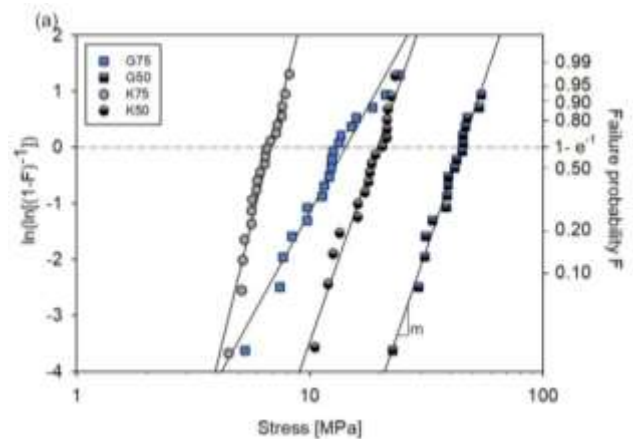
3.3 Scaffold Compressive Strength

Compressive strengths of the scaffolds, as displayed in the Weibull plot in Figure 4 (a), yielded results ranging from 6.75 - 44.7 MPa (compare Table 3) with lower porosity scaffolds exhibiting higher values. The fact that the rectilinear Grid structures withstand more than twice the amount of loading than the Kagome scaffolds, could be due to inhomogeneous stress distributions in the latter architectures. When regarding the stress-strain diagrams in Figure 4 (b), one can see pronounced discontinuities for both Kagome structures. These so called pop-in events have been extensively characterized for components with small heterogeneous zones such as in layered composite materials where cracks can be arrested when reaching a tougher material [63,64] and could have a similar origin in the present scaffolds when individual layers of unit cells fail under loading.

As an indication of the reliability of the scaffolds, Weibull moduli of ≥ 10 would be desired for ceramic materials [57]. These slightly lower values of 3.27 – 7.40 (compare Table 3) are, however, in accordance with values of 3 - 10 previously

found in literature for similar TCP structures [65] and could stem from reduced reproducibility when not working on bulk specimens.

Table 3: Weibull modulus and compressive Weibull strengths at e^{-1} failure probability of the scaffolds (n =18). No Weibull analysis was carried out for the non-porous 3x3x6 mm F0 structure, as specimen repetitions are not sufficient (for these, average with SD are given; n = 9).

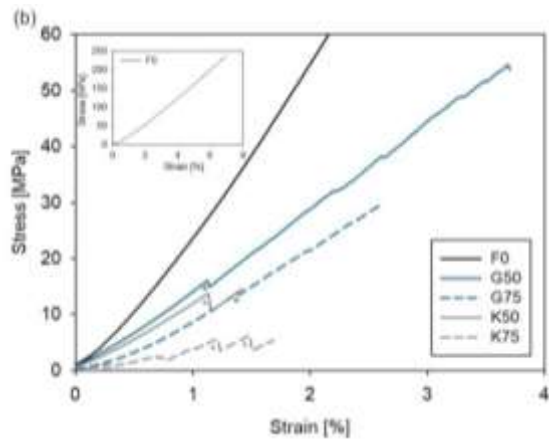| Sample	Weibull modulus	Compressive strength [MPa]
G75	3.27	14.2
G50	5.28	44.7
K75	7.40	6.75
K50	5.18	19.5
F0	-	235 ± 37

Figure 4: (a): Weibull plot of scaffolds in compression testing. Weibull modulus, m, attained from the slope of the linear regression and the compressive strength from the stress at e^{-1} failure probability (b): Representative stress-strain curves of scaffolds and of the non-porous F0 structure in compression. Distinct pop-in events marked with *.

When comparing to expected compressive strength values for bone at similar densities, as plotted in Figure 5, one can see that the scaffolds are not as strong as compact bone, which is often stated to be in the range of 100 - 180 MPa [9], [10]. However, literature values of comparable scaffolds, i.e. of pure β-TCP structures with pore sizes larger than 50 µm, also do not reach these desired strengths. To our best knowledge, especially the Grid structure has noticeably higher compressive strengths than any similar scaffolds found in literature, which range from 1 MPa [66] to 20 MPa [27], compare Figure 5.
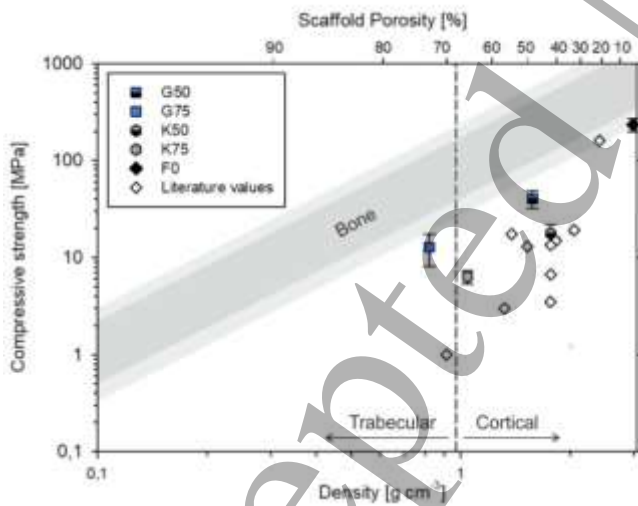

Figure 5: Compressive strengths of manufactured scaffolds in dependence of scaffold porosity (top axis) compared to predictions for bone as a function of ash density (bottom axis). Upper limit was taken from [67] and lower limit from [68] with 30 % margin of error marked in light grey. Literature values of comparable β-TCP scaffolds were taken from [27,37,65,66,69–73]. Figure design adapted from [65].

3.4 Cell culture

3.4.1 Cell Growth and Morphology

Seeding efficiency of the murine pre-osteoblastic cells, as seen from DNA amount after 1 day of cell culture, shown in Figure 6 (a), was at an average of 20 ± 2 % for the 3D scaffolds. While this limits the comparability to the 2D control conditions (supplementary Figure 1) seeded on tissue culture plastic, the more than two-fold increase of seeding efficiency of the scaffolds when compared to the 8 % of seeded cells adhering to the non-porous β-TCP cubes is advantageous.

After seeding, cell growth could be observed until day 7 of the experiment and the cells maintained that amount at day 14, as evident from the quantification in Figure 6 (a). When comparing the individual scaffold types, it appears that a larger DNA content was found on higher porosity Kagome scaffolds than on lower porosity Grid scaffolds. These trends are, however, not statistically significant. It is, thus, inferable that all scaffolds are compatible to the cells, which do not only adhere and grow on the TCP support but also change their morphology over the course of the experiment, as seen when regarding stained cells in Figure 6 (b) (see supplementary Figure 2 for all stained scaffolds).
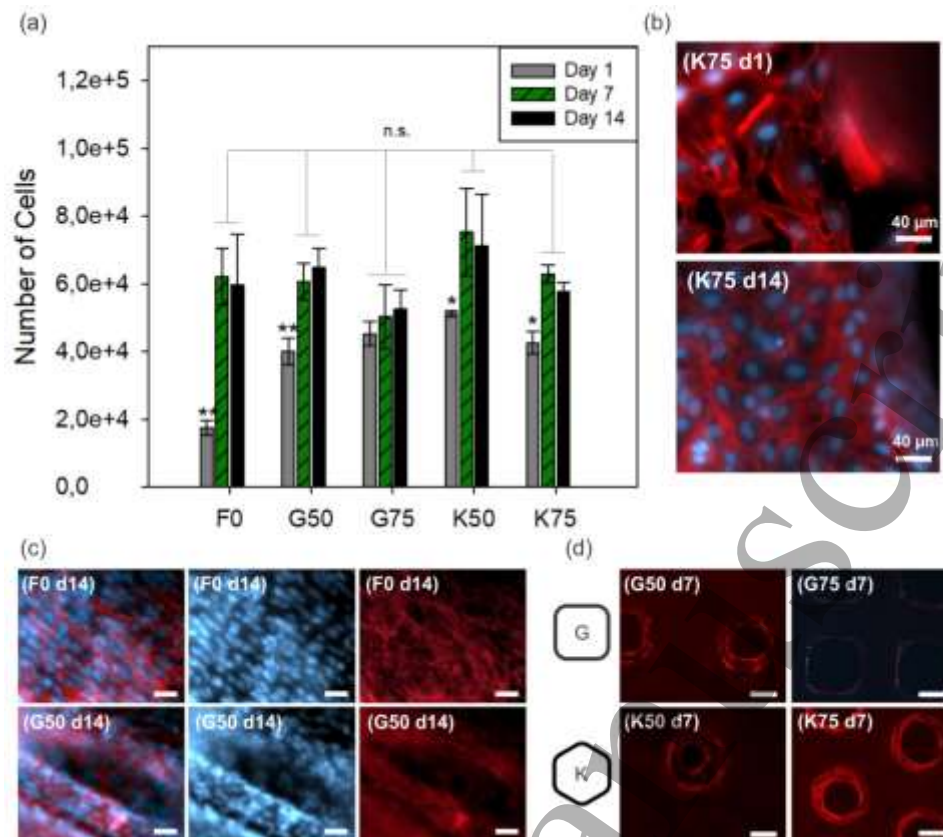
8

Figure 6: (a): Cell number from DNA quantification of the different 3D scaffolds in osteogenic medium; n = 3, with SD, n.s. for no statistically significant difference, * for P ≤ 0.005, and ** for P < 0.001. (b): Stained cells (ds-DNA visualized in blue and F-actin in red) of the Kagome 75 vol.% porous scaffold at 1 and 14 days of cell culture, scale bars are 40 µm. (c): Cell alignment at day 14 on the non-porous β-TCP specimen (F0) and on the 50 vol.% porosity Grid structure (G50), scale bars are 40 µm. (d): Overlay of a z-stack of confocal scanning microscopy images of F-actin stained scaffolds at day 7. Depth is 120 µm with one image every 20 µm, scale bars are 200 µm.

Due to the corresponding size scale of the 20 µm layers originating from the additive manufacturing process, alignment of cell nuclei was observed along these grooves [74], as depicted in Figure 6 (c). Larger scale ridges originating from pixilation due to the digital micro mirror device cause alignment primarily of the actin filaments. Both of these phenomena could be advantageous to cell adhesion and could have further effects on the cell's phenotype or differentiation behaviour [75].

F-actin growth into the pores, as shown in confocal fluorescence images in Figure 6 (d), appears to be more extensive for the hexagonal Kagome pores than for the cuboid Grid pores. Although this trend was not quantified, it is in accordance with curvature driven tissue growth previously described for MC3T3-E1 cells on HA [76].

3.4.2 ALP Activity and Collagen Deposition

In order to preliminarily asses osteogenic behaviour, ALP activity was investigated and quantified compare Figure 7 (a).

While 2D conditions had maximum ALP activity at day 7 (compare supplementary Figure 1), the maximum of the 3D scaffolds is delayed by a week and increased by a factor of > 2, when normalized to DNA. The porous scaffolds had elevated activity already 1 day after seeding and ALP activity remained high throughout the entire experiment. This could be explained by inhomogeneous seeding resulting in inconsistent areas of confluency and thereby in a broader range of onset-time of differentiation. The higher ALP activity especially for high porosity scaffolds does, however, strongly indicate osteogenic differentiation.

Total collagen deposition (Figure 7 (b) and (c)) indicates formation of ECM. Three times as much collagen was deposited by cells in osteogenic medium than in basal medium, as discernible from the 2D control in supplementary Figure 1. Furthermore, cells on 3D porous scaffolds deposited 1.5 – 1.7 times as much collagen as cells in 2D wells at day 14.
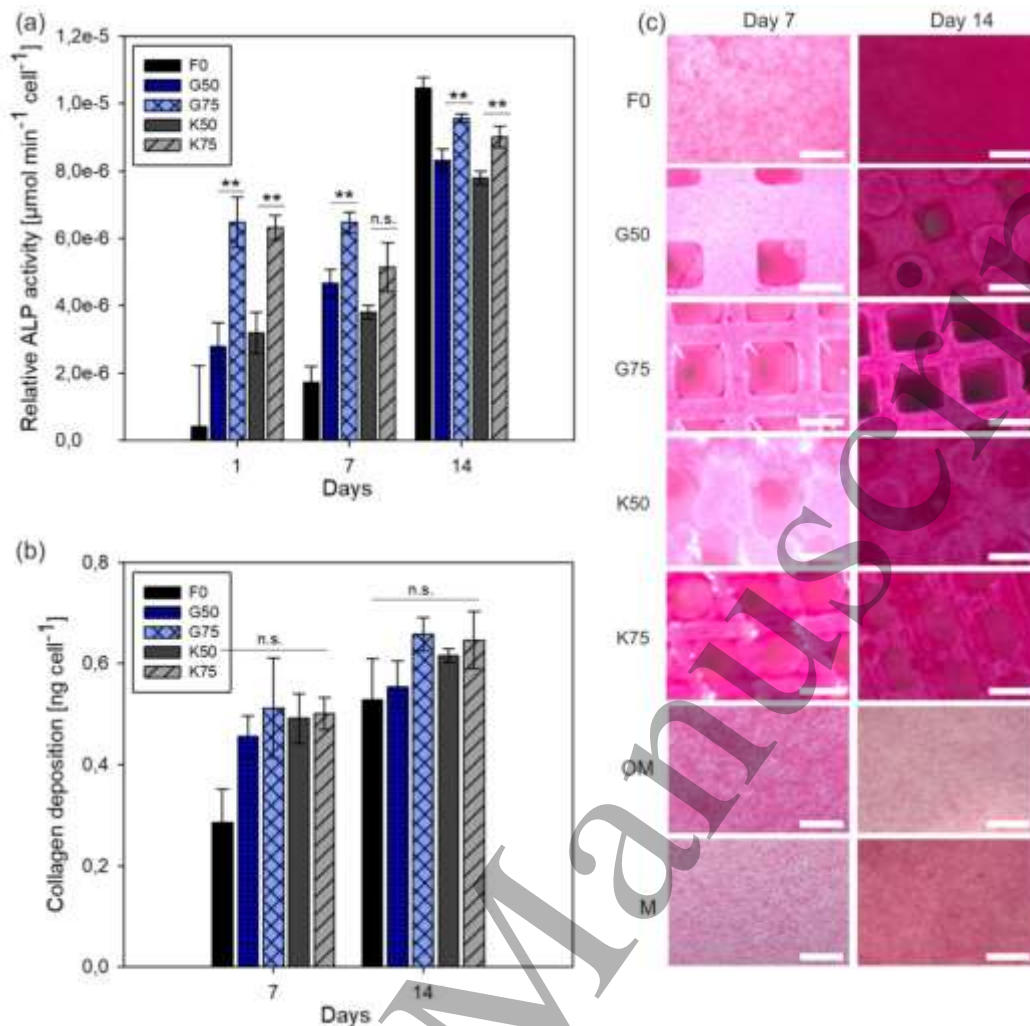
Figure 7: (a): ALP activity normalized to cell number on (b): Total collagen deposition normalized to cell number. Both are on 3D scaffolds in osteogenic medium. n = 3, with SD, n.s. for no statistically significant difference, ** for P < 0.001. (c): Light microscopy images of stained collagen, scale bars are 400 µm.

Both scaffold types support cell growth until day 14 with pronounced alignment along manufacturing layers and confirmed ALP activity as well as collagen deposition. Although the hexagonal architectures appear to have larger amount of cell growth, no statistically significant differences in cellular behaviour can be found to the rectilinear types. The effect of scaffold porosity is limited to the higher ALP activity in more porous structures.

4. Conclusion

High purity β-TCP scaffolds without carbon contamination or amorphous components and with relative strut densities up to 99.5 % could be manufactured with the DLP-based additive manufacturing system. Geometrical reproducibility was validated and found to be superior for the Grid structure than for the Kagome architecture, putatively due to its rectilinear nature. Correspondingly, the higher compressive strength by more than a factor of 2 when compared to the hexagonal

scaffolds is advantageous. While not quite reaching values of cortical bone [9–11], the through porosity tuneable compressive strengths of up to 44.7 MPa clearly exceed literature values for similar scaffolds [65,66,69–73]. Furthermore, the TCP scaffolds provide cellular compatibility and osteogenic differentiation of cells is indicated. The DLP process does not negatively impact the attained results and it, as well as the utilized material, can therefore be considered as biocompatible.

Thus, the presently manufactured β-TCP structures are promising for applications in bone regeneration as scaffolds and could also be employed as a starting point for composite structures. For instance in approaches where a ceramic framework is coated or impregnated with a polymer [66,72,77–79], a solid and reproducible scaffold foundation, such as described in the present paper is vital.

NA

References

[1]   Yuan H, Fernandes H, Habibovic P, de Boer J, Barradas A M C, de Ruiter A, Walsh W R, van Blitterswijk C A and de Bruijn J D 2010 *Proc. Natl. Acad. Sci. U. S. A.* **107** 13614–9

[2]   Kausar H and Kishore R N 2013 *Int. J. Pharm. Pharm. Sci.* **5** 30–2

[3]   Vallet-Regí M and Ruiz-Hernández E 2011 *Adv. Mater.* **23** 5177–218

[4]   Liu J, Willför S and Mihranyan A 2017 *Carbohydr. Polym.* **172** 11–9

[5]   O'Brien F J 2011 *Mater. Today* **14** 88–95

[6]   Ghassemi T, Shahroodi A, Ebrahimzadeh M H, Mousavian A, Movaffagh J and Moradi A 2018 *Arch. bone Jt. Surg.* **6** 90–9

[7]   Kroeze R, Helder M, Govaert L and Smit T 2009 *Materials (Basel).* **2** 833–56

[8]   Chan B P and Leong K W 2008 *Eur. Spine J.* **17 Suppl 4** 467–79

[9]   Wagoner Johnson A J and Herschler B A 2011 *Acta Biomater.* **7** 16–30

[10]   Carter D R and Hayes W C 1976 *Science* **194** 1174–6

[11]   Schaffler M B and Burr D B 1988 *J. Biomech.* **21** 13–6

[12]   Karageorgiou V and Kaplan D 2005 *Biomaterials* **26** 5474–91

[13]   Roseti L, Parisi V, Petretta M, Cavallo C, Desando G, Bartolotti I and Grigolo B 2017 *Mater. Sci. Eng. C* **78** 1246–62

[14]   Kuboki Y, Jin Q and Takita H 2001 *J. Bone Joint Surg. Am.* **83–A Suppl 1** S105-15

[15]   Woodard J R, Hilldore A J, Lan S K, Park C J, Morgan A W, Eurell J A C, Clark S G, Wheeler M B, Jamison R D and Wagoner Johnson A J 2007 *Biomaterials* **28** 45–54

[16]   Feng B, Jinkang Z, Zhen W, Jianxi L, Jiang C, Jian L, Guolin M and Xin D 2011 *Biomed. Mater.* **6** 015007

[17]   Ghayor C and Weber F E 2018 *Front. Physiol.* **9** 960

[18]   Shi C, Yuan Z, Han F, Zhu C and Li B 2016 *Ann. Jt.* **1** 27–27

[19]   Dhandayuthapani B, Yoshida Y, Maekawa T and Kumar D S 2011 *Int. J. Polym. Sci.* **2011** 1–19

[20]   Liu X and Ma P X 2004 *Ann. Biomed. Eng.* **32** 477–86

[21]   Baino F, Hamzehlou S and Kargozar S 2018 *J. Funct. Biomater.* **9**

[22]   Fu Q, Saiz E, Rahaman M N and Tomsia A P 2011 *Mater. Sci. Eng. C. Mater. Biol. Appl.* **31** 1245–56

[23]   Samavedi S, Whittington A R and Goldstein A S 2013 *Acta Biomater.* **9** 8037–45

[24]   Sheikh Z, Abdallah M-N, Hanafi A A, Misbahuddin S, Rashid H and Glogauer M 2015 *Mater. (Basel, Switzerland)* **8** 7913–25

[25]   Bell L C, Mika H and Kruger B J 1978 *Arch. Oral Biol.* **23** 329–36

[26]   Slots C, Jensen M B, Ditzel N, Hedegaard M A B, Borg S W, Albrektsen O, Thygesen T, Kassem M and Andersen M Ø 2017 *Dent. Mater.* **33** 198–208

[27]   Feng S, He F and Ye J 2017 *Ceram. Int.* **43** 6778–85

[28]   Yang S, Yang H, Chi X, Evans J R G, Thompson I, Cook R J and Robinson P 2008 *Mater. Des.* **29** 1802–9

[29]   Yang H, Yang S, Chi X and Evans J R G 2006 *J. Biomed. Mater. Res. Part B Appl. Biomater.* **79B** 116–21

[30]   Trombetta R, Inzana J A, Schwarz E M, Kates S L and Awad H A 2017 *Ann. Biomed. Eng.* **45** 23–44

[31]   Shuai C, Li P, Liu J and Peng S 2013 *Mater. Charact.* **77** 23–31

[32]   Ma B, Lin L, Huang X, Hu Q and Fang M 2006 *Knowledge Enterprise: Intelligent Strategies in Product Design, Manufacturing, and Management* (Springer US) pp 710–6

[33]   Sing S L, Yeong W Y, Wiria F E, Tay B Y, Zhao Z, Zhao L, Tian Z and Yang S 2017 *Rapid Prototyp. J.* **23** 611–23

[34]   Bertrand P, Bayle F, Combe C, Goeuriot P and Smurov I 2007 *Appl. Surf. Sci.* **254** 989–92

[35]   Mancuso E, Alharbi N, Bretcanu O A, Marshall M, Birch M A, McCaskie A W and Dalgarno K W 2017 *Proc. Inst. Mech. Eng. Part H J. Eng. Med.* **231** 575–85

[36]   Ke D and Bose S 2018 *Addit. Manuf.* **22** 111–7

[37]   Tarafder S, Balla V K, Davies N M, Bandyopadhyay A and Bose S 2013 *J. Tissue Eng. Regen. Med.* **7** 631–41

[38]   Putlyaev V I, Evdokimov P V., Safronova T V., Klimashina E S and Orlov N K 2017 *Inorg. Mater.* **53** 529–35

[39]   Lee J-B, Maeng W-Y, Koh Y-H and Kim H-E 2018 *Mater. (Basel, Switzerland)* **11**

[40]   de Blas Romero A, Pfaffinger M, Mitteramskogler G, Schwentenwein M, Jellinek C, Homa J, D??az Lantada A and Stampfl J 2017 *Int. J. Adv. Manuf. Technol.* **88** 1547–55

[41]   Schwentenwein M and Homa J 2015 *Int. J. Appl. Ceram. Technol.* **12** 1–7

[42]   Zeng Y, Yan Y, Yan H, Liu C, Li P, Dong P, Zhao Y and Chen J 2018 *J. Mater. Sci.* **53 6291–301**

[43]   Zok F W, Latture R M and Begley M R 2016 *J. Mech. Phys. Solids* **96** 184–203

[44]   Schwentenwein M, Schneider P and Homa J 2014 *Adv. Sci. Technol.* **88** 60–4

[45]   Waheed S, Cabot J M, Macdonald N P, Lewis T, Guijt R M, Paull B and Breadmore M C 2016 *Lab Chip* **16** 1993–2013

[46]   Wurst J C and Nelson J A 1972 *J. Am. Ceram. Soc.* **55** 109–109

[47]   Anon 2004

[48]   Rodriguez-Carvajal J 1993

[49]   Lazoryak B I, Oralkov S Y, Golubev V N and Zhdanova A N 1989 *Russ. J. Inorg. Chem* **34** 968–70

[50]   Arsen'ev P A, Evdokimov A A, Smirnov S A, Filimonova M R, Tsekhanovich V M and Sheinin M Y 1992 *Russ. J. Inorg. Chem* **37** 1366–8

[51]   Anon 2015

[52]   Quinn J B and Quinn G D 2010 *Dent. Mater.* **26** 135–47

[53]   Griffin M, Nayyer L, Butler P E, Palgrave R G, Seifalian A M and Kalaskar D M 2016 *Nanomedicine* **12** 1725–33

[54]   Gentry S P and Halloran J W 2015 *J. Eur. Ceram. Soc.* **35** 1895–904

[55]   Bouslama N, Ayed F Ben and Bouaziz J 2008 *Phys. Procedia* **2** 1441–8

[56]   Davidge R W 1969 *Contemp. Phys.* **10** 105–24

[57]   Industrie V der K 2003 *Brevier Technische Keramik* (Lauf: Fahner Verlag)

[58]   Yoshii E 1997 *J. Biomed. Mater. Res.* **37** 517–24

[59]   Melchels F P W, Feijen J and Grijpma D W 2010 *Biomaterials* **31** 6121–30

[60]   Chusuei C C, Goodman D W, Van Stipdonk M J, Justes D R and Schweikert E A 1999 *Anal. Chem.* **71** 149–53

[61]   Lu H B, Campbell C T, Graham D J and Ratner B D 2000 *Anal. Chem.* **72** 2886–94

[62]   Mallick K 2014 *Bone substitute biomaterials* (Cambridge: Woodhead Publishing Limited) pp 180–200

[63]   BERMEJO R, TORRES Y, SANCHEZHERENCIA A, BAUDIN C, ANGLADA M and LLANES L 2006 *Acta Mater.* **54** 4745–57

[64]   Fu K, Tang Y and Chang L 2016 *Fracture Mechanics - Properties, Patterns and Behaviours* (InTech)

[65]   Miranda P, Pajares A, Saiz E, Tomsia A P and Guiberteau F 2008 *J. Biomed. Mater. Res. Part A* **85A** 218–27

[66]   Zairani N A S, Jaafar M, Ahmad N and Abdul Razak K 2016 *Ceram. Int.* **42** 5141–7

[67]   Hernandez C ., Beaupré G ., Keller T . and Carter D . 2001 *Bone* **29** 74–8

[68]   Keller T S 1994 *J. Biomech.* **27** 1159–68

[69]   Feng P, Wei P, Shuai C and Peng S 2014 *PLoS One* **9** e87755

[70]   Metsger D S, Rieger M R and Foreman D W 1999 *J. Mater. Sci. Mater. Med.* **10** 9–17

[71]   Feng Y-F, Wang L, Li X, Ma Z-S, Zhang Y, Zhang Z-Y and Lei W 2012 ed A Pandit *PLoS One* **7** e49955

[72]   Deschamps I S, Magrin G L, Magini R S, Fredel M C, Benfatti C A M and M Souza J C 2017 *Eur. J. Dent.* **11** 496–502

[73]   Tian Y, Lu T, He F, Xu Y, Shi H, Shi X, Zuo F, Wu S and Ye J 2018 *Colloids Surfaces B Biointerfaces* **167** 318–27

[74]   Raimbault O, Benayoun S, Anselme K, Mauclair C, Bourgade T, Kietzig A-M, Girard-Lauriault P-L, Valette S and Donnet C 2016 *Mater. Sci. Eng. C* **69** 311–20

[75]   Lee H-J, Lee J, Lee J-T, Hong J-S, Lim B-S, Park H-J, Kim Y-K and Kim T-I 2015 *J. Periodontal Implant Sci.* **45** 120

[76]   Rumpler M, Woesz A, Dunlop J W C, Van Dongen J T and Fratzl P

[77]   Flauder S, Sajzew R and Müller F A 2015 *ACS Appl. Mater. Interfaces* **7** 845–51

[78]   Martínez-Vaázquez F J, Perera F H, van der Meulen I, Heise A, Pajares A and Miranda P 2013 *J. Biomed. Mater. Res. Part A* n/a-n/a

[79]   Feng S, He F and Ye J 2018 *Mater. Sci. Eng. C* **82** 217–24